International Journal of Solids and Structures 51 (2014) 3196–3208

Contents lists available at ScienceDirect

International Journal of Solids and Structures

journal homepage: www.elsevier.com/locate/ijsolstr

Wedge-shaped fracturing in the pull out of FRP stiffeners from quasi-brittle substrates

Roberto Ballarini [a,*], Annalisa Franco [b], Gianni Royer-Carfagni [b]

[a] Department of Civil Engineering, University of Minnesota, 500 Pillsbury Drive S.E., Minneapolis, MN 55455-0116, USA
[b] Department of Industrial Engineering, University of Parma, Parco Area delle Scienze 181/A, I 43100 Parma, Italy

ARTICLE INFO

Article history:
Received 20 February 2014
Received in revised form 19 April 2014
Available online 27 May 2014

Keywords:
Fiber Reinforced Polymer (FRP)
Stiffener
Pull-out test
Substrate cracking
Inclined crack propagation
Elasticity
Complex potential
Distributed dislocations

ABSTRACT

Fiber-Reinforced-Polymer (FRP) strips can be glued to the surface of concrete or masonry structures to improve their strength. Pull-out tests on FRP bonds have shown a progressive failure of the adhesive joint involving early-stage cracking parallel to the axis of the FRP stiffener, and an inclined crack initiating at the free end of the stiffener and extending into the quasi-brittle substrate in the latest stage. The subsurface crack produces a characteristic wedge-shaped spall. There is no consensus on the reasons for the transition from cracking along the bond to cracking within the substrate. Therefore a Linear Elastic Fracture Mechanics model problem is presented here that accounts for and provides improved understanding of the formation of the subsurface crack. The boundary value problem is solved analytically using the distributed dislocation technique. Competition between crack extension along the adhesive joint and into the substrate is quantified using a quantized crack propagation criterion, whereby the crack does not advance in infinitesimal continuous increments, but instead in finite steps of length comparable to the characteristic dimensions of the material microstructure. The model predicts results that are in good agreement with experimental evidence.

1. Introduction

The use of Fiber Reinforced Polymers (FRP) to repair and refurbish buildings and bridges is ever-increasing. A noteworthy application involves a wet lay-up procedure with epoxy resins to bond FRP strips or plates to the external surfaces of concrete and masonry flexural elements to increase their bending strength. The popularity of this technique has inspired supporting research that has focused primarily on the characterization of the mechanical performance of the bonded joint. Experiments have provided a wealth of evidence that the dominant failure mode is debonding within the adhesive joint, typically occurring a few millimeters below the adhesive interface. Failure modes such as plate-end debonding are regarded as *local failures* and have not received significant attention. However, understanding the *whole* process of debonding and the local failure modes is of importance to the prediction of the *ultimate flexural capacity* of the reinforced structure, in particular when it is subjected to seismic actions or accidental overloads.

A large number of experiments have been conducted in order to analyze and better understand the debonding phenomenon (Chen and Teng, 2001). Among the various experimental set-ups, simple pull-out tests are the most popular. These tests involve a long stiffener,[1] bonded to a quasi-brittle substrate, that is gradually pulled at one end. As also evidenced in Yuan et al. (2004), the failure is characterized by the formation of a cohesive (process) zone, where prior to neat separation a relative slip between stiffener and substrate occurs at non-zero shear stress. The progression of the process zone, which exhibits the distinct phases represented schematically in Fig. 1, defines the gross response of the stiffener in the pull-out test. In order to qualitatively describe the debonding phenomenon in all of its phases, recent works (Franco and Royer-Carfagni, 2013; Franco and Royer-Carfagni, 2014a,b) have considered the contact problem between an elastic stiffener and an elastic half-space. Unlike earlier analyses of such configurations where the substrate is supposed rigid, these works *analytically* demonstrated the role played by the deformation of both adherents, in agreement with previous numerical investigations (Freddi and Savoia, 2008; Marfia et al., 2011; Grande et al., 2011).

* Corresponding author. Tel.: +1 (612)625 2148; fax: +1 (612)626 7750.
E-mail addresses: broberto@umn.edu (R. Ballarini), annalisa.franco@unipr.it (A. Franco), gianni.royer@unipr.it (G. Royer-Carfagni).

[1] Long stiffeners are stiffeners whose length is greater than the effective bond length, i.e., the length beyond which there is no further increase of the load carrying capacity of the joint (Franco and Royer-Carfagni, 2014a).

http://dx.doi.org/10.1016/j.ijsolstr.2014.05.015
0020-7683/

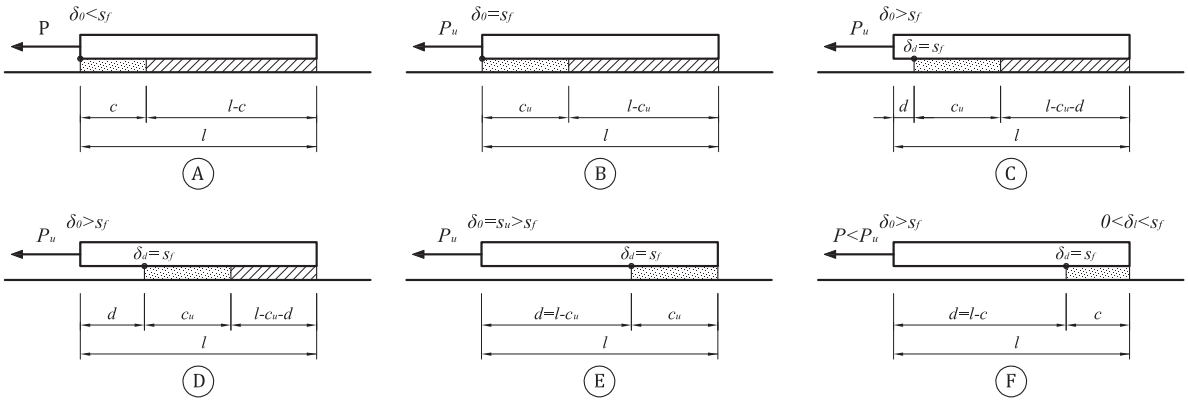

Fig. 1. Schematic representation of the debonding process for long stiffeners. (Franco and Royer-Carfagni, 2014a).

The process zone, represented by the etched rectangle of length c in Fig. 1A, nucleates at the loaded end of the stiffener, and it progresses in a stable manner until it reaches a critical length, indicated by c_u in Fig. 1B. The maximal length c_u is reached when the relative slip δ_0 at the loaded end of the bond reaches the critical crack sliding displacement, s_f, one of the parameters that defines the shear stress-relative slip constitutive relationship that governs the cohesive zone. Debonding initiates at this stage, at the critical value P_u of the applied load. As the stiffener is pulled further its displacement δ_0 relative to the substrate exceeds the limit value s_f and delamination begins. During this phase, corresponding to Fig. 1C and D, the length c_u does not change appreciably but simply translates as the delamination propagates along the interface and reaches the opposite free end. It was demonstrated (Franco and Royer-Carfagni, 2014a,b) that the resultant of the shear stress in the cohesive zone equilibrates in practice all of the applied force P, and thus the pull out force remains almost constant and equal to P_u during the delamination process.

When the cohesive zone approaches the free end of the stiffener (Fig. 1E), a strain-softening phase begins. Henceforth the length of the cohesive zone decreases, causing a reduction of the strength of the bond. This phase, sketched in Fig. 1F, is often associated with a *snapback* response that could not be captured under displacement control. Eventually the FRP stringer completely separates from the substrate. Remarkably, such a failure is characterized by the formation of a characteristic *wedge-shaped* spall, as shown in Fig. 2 for a FRP-to-concrete bond. Experiments (Biolzi et al., 2013; Carrara et al., 2011, 2013; Grande et al., 2011) have evidenced that the width of this bulb is approximately equal to the width of the FRP lamina. However, its length is independent of the initial length of the reinforcement (Biolzi et al., 2013) as confirmed in Fig. 2, where various bond lengths are compared. This phenomenon is true not only for concrete, but also for masonry.

The stage at which the bulb-like spall forms corresponds to a very small bond length, of the order of 30–50 mm, and is associated with phase F of Fig. 1. The bulb is isolated by an inclined crack that initiates at the free end of the stiffener, and whose extension eventually leads to the complete separation of a portion of material from the substrate. To the authors' knowledge, there have been just a few attempts to model this phenomenon (Marfia et al., 2011). Thus the present study.

A key hypothesis made here that enables interpretation of the phenomenon is that fractures do not progress continuously and uniformly, but in discrete steps. In other words, there is a *quantized* length for crack propagation, that is attributed to the fact that the characteristic dimensions of the experiment are comparable to those of the microstructure of the substrate material. For the case of artificial conglomerates like concrete, the finite length crack increment is of the same order as the characteristic size of the constituent aggregates. The justification for the hypothesis is that the aggregate represents the most brittle constituent in the concrete mass; when the stress intensity factor of a crack within a portion of an aggregate reaches a critical value, the crack is prone to extend through the whole grain, rather than arrest within it. The granular microstructure of the substrate prevents the possibility of a *continuous* propagation of cracks. This fact is confirmed by experimental evidence. Fig. 3 shows a concrete surface from which an adherent FRP strip was pulled off. Notice the presence of well-marked grooves on the surface that reflect the discrete steps taken by the advancing crack front. A theory of "quantized fracture mechanics" has been recently proposed in Pugno and Ruoff (2004) to interpret the size effect in solids made of quasi brittle materials.

Under reasonable simplifying assumptions, a model problem in linear elasticity is now proposed. Of course, as clearly evidenced in Pellegrino et al. (2008), the debonding process has a three-dimensional character since it involves deformations also along the width

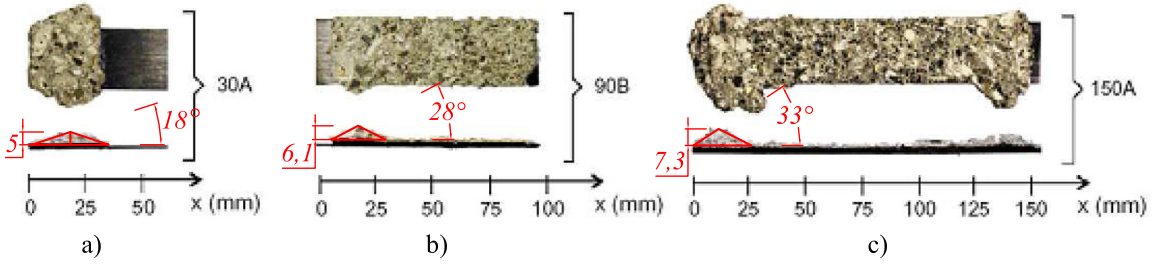

Fig. 2. Wedge-shaped detached portions of the substrate in FRP-to concrete bonds with different initial bond lengths, as *per* Carrara et al. (2011). Initial bond length: (a) $l = 30$ mm, (b) $l = 90$ mm; (c) $l = 150$ mm.

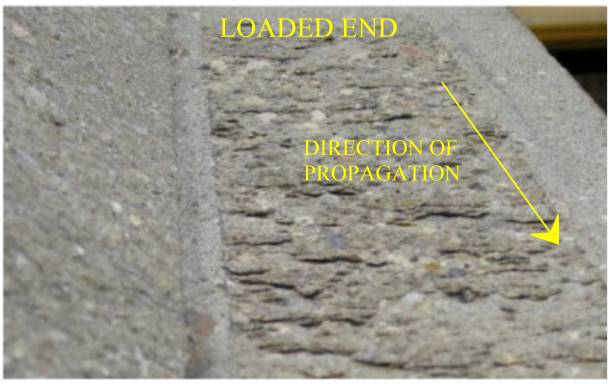

Fig. 3. Detail of the surface of a concrete support after debonding of the FRP strip (Mazzotti et al., 2009).

of the substrate. However, our aim here is to present an analytical study that, despite its simplicity, can evidence the key-aspects and the reasons for the occurrence of subsurface crack propagation. Having in mind an averaged-in-the-width 2-D approach, the stiffener is assumed to transmit shear stresses to a substrate modeled as a homogeneous isotropic elastic half-plane in generalized plane stress. The elastic fields are found by means of the distributed dislocation technique proposed in Eshelby et al. (1951) and developed by different authors (Dundurs, 1969; Hills, 1996; Ballarini et al., 1987; Ballarini et al., 1990; He and Hutchinson, 1988). The formulation of the propagation of a crack at the free end of the stiffener relies on the superposition of two effects: (i) the effect of tangential forces *per* unit area on the surface of the half plane and (ii) the effect of distributed edge dislocations along the crack reference configuration. The condition that the crack surfaces are traction-free furnishes an integral equation, which is solved using the properties of Chebyshev polynomials.

In the proposed model, two mechanisms of degradation are considered; (a) failure of the adhesive joint, which progresses at the stiffener-substrate interface when the corresponding shear stress is greater than the strength of the interface; (b) inclined cracking, which can develop in the substrate when the strain energy release associated with its (quantized) propagation is greater than the corresponding fracture energy of the material. From the competition between the two mechanisms one can evaluate when the inclined crack starts to form and the characteristic angle of the wedge-shaped bulb. The proposed model problem represents a simple and intuitive tool to investigate this peculiar phenomenon and provides results that are in very good qualitative agreement with experiments drawn from the technical literature.

2. The model problem

A simple Linear Elastic Fracture Mechanics model amenable of an analytical treatment is now presented. It relies on a few simplifying assumptions.

2.1. Preliminary considerations

The detachment of a bulb from the substrate occurs in the latest stage of the debonding process, where the surviving bond length is very small, of the order of 30–50 mm. In the schematic representation of Fig. 1, this stage is associated with phase F. The characteristic wedge-like shape of the bulb, represented in Fig. 2, is due to the nucleation of an inclined crack that initiates at the free end of the stiffener, and eventually induces the complete separation of that portion of the substrate.

In general, the stiffener is a very thin strip or plate, with negligible bending stiffness. Therefore, peeling stresses at the interface are absent because the stiffener is not able to equilibrate transverse loads during small deformations. Thus the only relevant contact stresses are the shear stresses acting along the stiffener-substrate interface (Franco and Royer-Carfagni, 2014a). Direct consideration of such stresses by-passes the problems usually associated with the elastic modeling of a bi-material interface and the complex stress singularities there occurring (Le et al., 2010). There is general agreement that the strength of the adhesive joint can be characterized through a shear-bond-stress "τ" *vs.* relative-slip "s" constitutive law. The $\tau - s$ curve is evaluated by measuring experimentally the strain in the stiffener and the substrate (Ali-Ahmad et al., 2006). The typical response is illustrated in Fig. 4: the quasi-linear branch leading to the peak stress is followed by a strain-softening phase that ends at the zero-stress level associated with complete debonding. This curve can be approximated by three straight lines (CNR-DT/200, 2004); an ascending branch up to the peak stress τ_f; a linear strain-softening phase approaching $s = s_f$ where $\tau = 0$ and, finally, a zero-stress *plateau*. In certain cases, to interpret the gradual debonding process, it is sufficient to consider a simple step-wise approximation of such a constitutive law (Franco and Royer-Carfagni, 2014a,b) with equal fracture-energy G_f and critical crack sliding displacement s_f, so that the maximum shear stress is $\tau_c = \frac{1}{2}\tau_f$. But if the bond length is very small, as it is in the final stage of the debonding process, then the relative displacement at the extremities is moderate. Consequently, one can neglect the strain gradient and assume that the slip is uniform. The consequence is that the interfacial shear stress transmitted by the stiffener to the substrate can be considered constant over the entire bond length.

The initiation of the inclined crack is sketched in Fig. 5(a) for a bond length that reaches the critical value l. Observe that when a crack of length a, inclined by the angle ω, forms at the free end of the stiffener, a wedge-shaped prism is formed within the substrate. This suggests that the substrate stiffness is locally degrading in the neighborhood of the crack.

As a first order approximation, the effect of the elastic deformation of the substrate can be modeled by a set of shear springs à *là* Winkler, which connect the stiffener to a support now supposed infinitely rigid. This scheme is represented in Fig. 5(b). But if a portion of the substrate locally yields because of the formation of the inclined crack, then the stiffness of the springs tends to zero in a neighborhood of such a portion. Consequently, there is a local release of the stiffener, that must be taken into account.

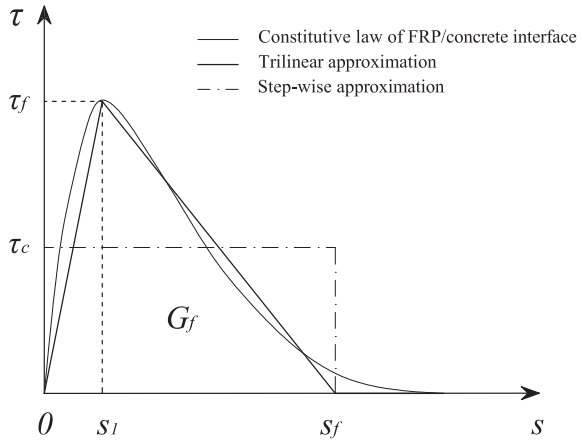

Fig. 4. Typical experimentally-measured shear-stress τ vs. slip s constitutive law at the interface; trilinear and step-wise approximations.

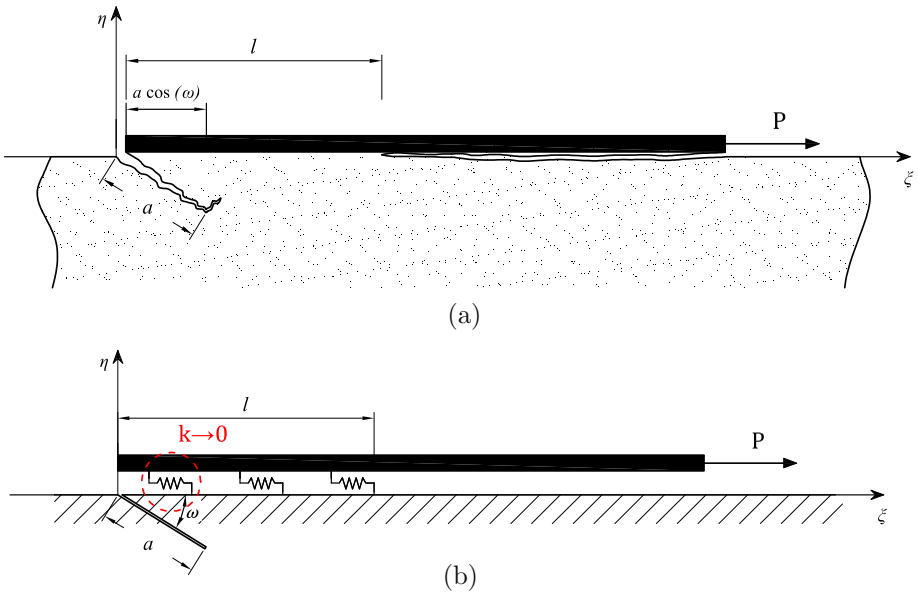

Fig. 5. A finite stiffener bonded to the boundary of a semi-infinite plate. (a) Edge crack forming at the free end of the stiffener; (b) Simplified scheme with a set of shear springs à *là* Winkler.

A quantitative interpretation is achieved by considering the problem of an elastic half plane in generalized plane stress, with a crack of length a inclined by the angle ω. A uniformly-distributed shear stress q is applied on the free surface of the half-space, for a length l starting from the crack origin, to represent the contact stress transmitted by the stiffener over its *whole* bond length. The elasticity problem is solved using the method presented in Section 2.2 and the corresponding solution is recorded in Appendix A. The normal component of strain ε_{rr} in the direction of the surface of the half-plane, derived according to Eqs. (A.7) and (A.12a), is drawn in Fig. 6 as a function of the normalized abscissa $\xi/(a\cos\omega)$, indicated in Fig. 5(a). Apart from a neighborhood of $\xi = 0$, the analytical solution is in perfect agreement with the results of numerical simulations performed with the FEM program Abaqus (ABAQUS, 2010), also reported in the same figure for the sake of comparison.

The analytical solution predicts a strain singularity at $\xi = 0^+$; then the strain remains almost constant for $0 < \xi/(a\cos\omega) < 1$. Moreover, one finds that the strain energy becomes infinite as the angle ω tends to zero. It should be observed that over the wedge-shaped portion isolated from the substrate by the inclined crack (Fig. 5(a)), the state of stress is similar to that associated with the Michell problem of a long wedge subjected to shear loading along one of the sides (Michell, 1899), as represented in Fig. 7. The solution by Michell, whose relevant results are given in Appendix A (Eqs. (A.11) and (A.12a)), prescribes a constant strain that fits very well with the analytical solution and the numerical experiments in the range $0 < \xi/(a\cos\omega) < 1$, as represented in Fig. 6. As $\omega \to 0$ the displacement becomes infinite and therefore the elastic strain energy becomes unbounded.

It is important to note that the strain over the portion $0 \leqslant \xi/a\cos(\omega) \leqslant 1$ is much higher (in absolute value) than in the remaining part of the bond length. For the case considered in Fig. 6, representative of a typical condition ($l = 52$ mm, $a = 15$ mm, $\omega = 30°$, $q = 3.85$ MPa), the strain in the neighborhood of the crack is more than five times higher than the strain in the remaining portion. Consequently, in the simplified scheme of Fig. 5(b), the stiffness of the springs on that left-hand-side portion would be about 20% of the stiffness of the others.

Deriving an analytical solution to the actual contact problem of an elastic stringer bonded to an elastic half space with an inclined crack is a formidable task that is not attempted here. Instead, with the aim at a qualitative description of the phenomenon, the following assumptions are made to achieve a reasonable first-order approximation:

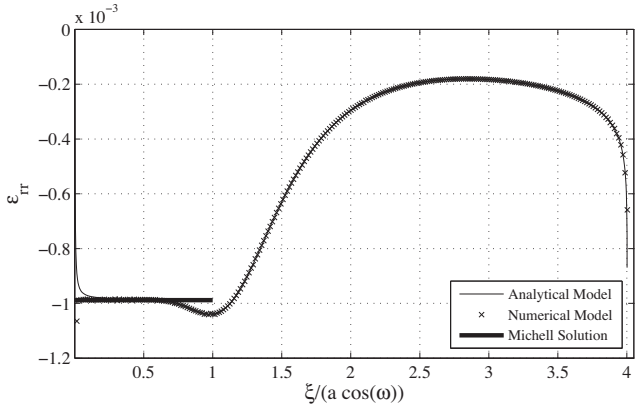

Fig. 6. Elastic half plane with an inclined crack, loaded by a uniformly distributed load for the whole bond length. Normal component of strain in the direction of the surface of the half-space, as a function of the normalized abscissa $\xi/(a\cos\omega)$. Elastic solution, numerical results, approximate Michell solution.

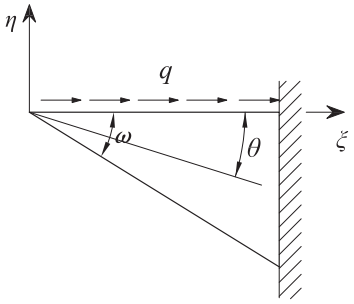

Fig. 7. Michell problem of a wedge, loaded along one side by shear stresses.

- the stringer is only able to transmit shear contact stresses because of its negligible bending stiffness;
- the shear contact stress is constant, because the actual bond length of the stringer in the latest stage of the debonding process is so small that one can assume that the stiffener-substrate relative slip is constant;
- the shear contact stress is null in the interval $0 \leqslant \xi/a\cos(\omega) \leqslant 1$; in fact, one can neglect the stiffness offered by the substrate in that portion because of the formation of the inclined crack.

In conclusion, the elasticity problem that will be considered is that represented in Fig. 8. Here, a linear-elastic, homogenous and isotropic half-plane in generalized plane stress, with an inclined crack initiating at $\xi = 0$, is loaded by an uniformly distributed shear stress q on the interval $a\cos(\omega) \leqslant \xi \leqslant l$.

Observe that all the aforementioned hypotheses are required, without exception, for a simple but complete description of the phenomenon. In particular, it is crucial to consider that there is a local weakening of the substrate in the neighborhood of the inclined crack. Here we have made the simplifying, quite drastic, assumption that the shear contact stress is null in the interval $0 \leqslant \xi/a\cos(\omega) \leqslant 1$. Of course, more refined considerations could be made, but the simplicity of the analytical solutions would be lost. Comparison with numerical experiments, where such simplifying assumption is not made, will be the subject of future studies.

2.2. Governing equations in linear elasticity theory

The elastostatics problem shown in Fig. 8 can be formulated in terms of the complex Muskhelishvili potentials (Muskhelishvili, 1975). With respect to a system of polar coordinates as in Fig. 9(a), centered at $\xi = \eta = 0$, the components of stress in polar coordinates can be expressed in terms of two analytic functions $\Phi(z)$ and $\Psi(z)$ of the complex variable $z = \xi + i\eta = re^{i\theta}$ as

$$\sigma_{rr} + \sigma_{\theta\theta} = 4\mathrm{Re}\,[\Phi(z)], \tag{2.1a}$$

$$\sigma_{\theta\theta} - \sigma_{rr} + 2i\sigma_{r\theta} = 2e^{2i\theta}[\bar{z}\Phi'(z) + \Psi(z)], \tag{2.1b}$$

$$\sigma_{\theta\theta} + i\sigma_{r\theta} = \Phi(z) + \overline{\Phi(z)} + e^{2i\theta}[\bar{z}\Phi'(z) + \Psi(z)], \tag{2.1c}$$

in which $i = \sqrt{-1}$, μ is the shear modulus, $\kappa = 3 - 4\nu$ for plane strain and $\kappa = (3-\nu)/(1+\nu)$ for generalized plane stress, and ν is Poisson's ratio. Moreover, $(\cdot)'$ denotes differentiation with respect to z and $\overline{(\cdot)}$ implies complex conjugation.

The normal and shear components of stress must be zero on the crack surfaces, i.e.,

$$\sigma_{\theta\theta} + i\sigma_{r\theta} = 0, \quad \text{for } \theta = -\omega, \quad 0 \leqslant r \leqslant a \tag{2.2}$$

and must agree with the boundary conditions on the surface of the half space.

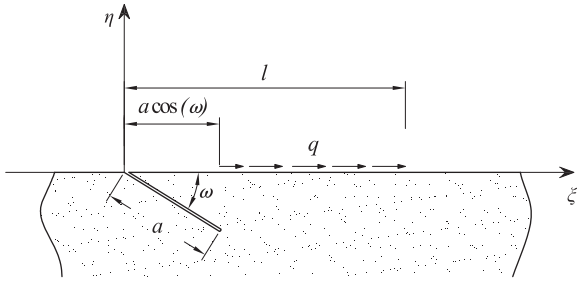

Fig. 8. Model problem for a finite stiffener bonded to the boundary of an elastic half-space, where an inclined fracture forms.

In the distributed dislocation approach, the problem can be reduced to that of an elastic half-plane containing a distribution of edge dislocations on $\theta = -\omega$, $0 \leqslant r \leqslant a$, as described in Fig. 9(a), and tangential stress $q(\xi)$ applied over the portion $\theta = 0$, $a\cos(\omega) \leqslant r \leqslant l$, as indicated in Fig. 9(b).

Eq. (2.2) can then be written as

$$(\sigma_{\theta\theta} + i\sigma_{r\theta})^{(d+q)} = (\sigma_{\theta\theta} + i\sigma_{r\theta})^{d} + (\sigma_{\theta\theta} + i\sigma_{r\theta})^{q} = 0, \quad \text{for } \theta = -\omega, \quad 0 \leqslant r \leqslant a, \tag{2.3}$$

where superscripts d and q indicate the contribution of dislocations and shear stresses, respectively.

2.2.1. Problem I: elastic half-plane with edge dislocations

Consider a straight crack of length a at an angle $\theta = -\omega$ in an elastic half plane $\eta < 0$, as indicated in Fig. 10. The functions $\Phi(z)$ and $\Psi(z)$ are holomorphic in this region. If z is a point of the lower half-plane, clearly $\bar{z}$ is its mirror image in the upper half-plane.

The solution of the problem of one edge dislocation in an elastic homogenous half-space is known (Dundurs, 1969). It can be represented in complex variables form using the analytic continuation procedure. The complex potentials given by

$$\Phi_{dw}(z) = \frac{\beta}{z - z_0}, \quad \Psi_{dw}(z) = \frac{\overline{\beta}}{z - z_0} + \frac{\beta\bar{z}_0}{(z - z_0)^2}, \tag{2.4}$$

define the elastic solution at any point z for a *dislocation* acting at point z_0 in a *whole* elastic plane. The constant β is defined as

$$\beta = \frac{\mu}{\pi i(\kappa + 1)}[b_r + ib_\theta]\frac{z_0}{|z_0|}, \tag{2.5}$$

where b_r and b_θ represent the radial and circumferential components of the Burgers vector.

These potentials produce non-zero tractions along the line representing the free surface of the half-plane. To clear these, an additional set of complex potentials are added. These are determined using the analytic continuation of (2.4) through the boundary of the half plane (Muskhelishvili, 1975). In conclusion, one finds that the potential Φ in the half plane $\mathrm{Im}(z) \leq 0$ reads

$$\Phi_{dc}(z) = -\overline{\Phi_{dw}(\bar{z})} - z\overline{\Phi'_{dw}(\bar{z})} - \overline{\Psi_{dw}(\bar{z})}, \tag{2.6}$$

using the notation $\overline{\Phi}(z) = \overline{\Phi(\bar{z})}$, and $\overline{\Phi}(\bar{z}) = \overline{\Phi(z)}$. For the particular case of a half plane with zero tractions on the boundary, using symmetry considerations, one can demonstrate (Muskhelishvili, 1975) that the expression (2.1c) can be simplified and results to be a function of the potential $\Phi(z)$ only. In particular, one finds

$$\sigma_{\theta\theta} + i\sigma_{r\theta} = \overline{\Phi(z)} + (1 - e^{-2i\omega})\Phi(z) + (\bar{z} - z)e^{-2i\omega}\Phi'(z) - e^{-2i\omega}\overline{\Phi}(z). \tag{2.7}$$

By setting in this expression $\Phi(z) = \Phi_{dw}(z) + \Phi_{dc}(z)$, as *per* (2.4) and (2.6), one obtains the desired solution.

The discrete dislocation at $z_0 = \rho e^{-i\omega}$ can be replaced by a distribution of dislocations, $B(\rho)d\rho$, of the form

$$B(\rho) = \frac{\mu}{\pi i(\kappa + 1)}\frac{\partial}{\partial\rho}[b_r + ib_\theta]e^{-i\omega}. \tag{2.8}$$

In this way, maintaining fixed ω and integrating over the length of the crack a, the relevant stresses on the radial line $z = re^{-i\omega}$ (Fig. 10) due to the distributed dislocations become

$$(\sigma_{\theta\theta} + i\sigma_{r\theta})^{d} = \int_0^a B(\rho)K_1(r,\rho)d\rho + \int_0^a \overline{B(\rho)}\left[\frac{2e^{-i\omega}}{r - \rho} + K_2(r,\rho)\right]d\rho, \tag{2.9}$$

where $K_1(r,\rho)$ and $K_2(r,\rho)$ are given in Appendix B.

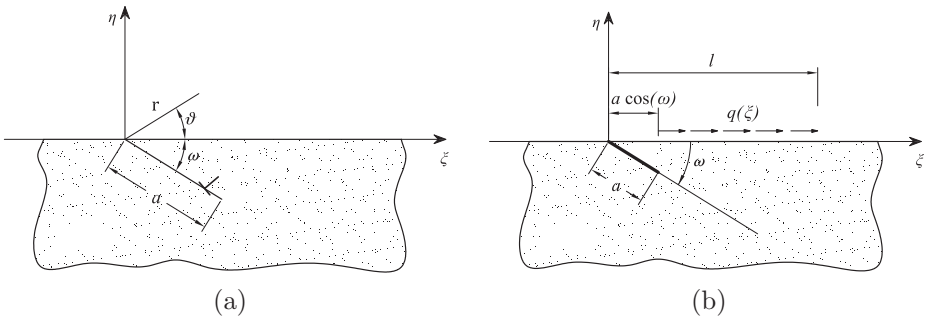

Fig. 9. Superposition effects: (a) distributed edge dislocation; (b) effect of surface tangential stress.

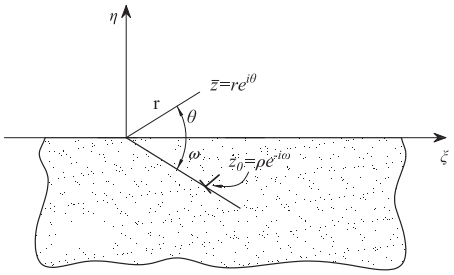

Fig. 10. An edge dislocation in a half space. Representative variables.

2.2.2. Problem II: elastic half-plane under surface tangential stress

In the problem of Fig. 11, a distribution of shear stresses $q(\xi)$, positive if directed towards the positive ξ-axis, is applied on the surface over the length $l_c = l - a\cos\omega$.

The complex potentials for the *uncracked* half plane are given by

$$\Phi_q(z) = -\frac{1}{2\pi}\int_{a\cos\omega}^{l}\frac{q(\xi)}{\xi - z}d\xi, \tag{2.10a}$$

$$\Psi_q(z) = \frac{1}{2\pi}\int_{a\cos\omega}^{l}\frac{q(\xi)}{\xi - z}d\xi - \frac{1}{2\pi}\int_{a\cos\omega}^{l}\frac{q(\xi)}{(\xi - z)^2}\xi d\xi. \tag{2.10b}$$

The relevant stresses on the radial line $z = re^{-i\omega}$ ($\bar{z} = re^{i\omega}$) of Fig. 11, can be obtained by substituting Eq. (2.10) in (2.7), to give

$$(\sigma_{\theta\theta} + i\sigma_{r\theta})^q = \frac{1}{2\pi}\left[\int_{a\cos\omega}^{l}\overline{q(\xi)}H_1(r,\xi)d\xi + \int_{a\cos\omega}^{l}q(\xi)H_2(r,\xi)d\xi\right], \tag{2.11}$$

where $H_1(r,\xi)$ and $H_2(r,\xi)$ are given in Appendix B.

3. Solution of the elastic problem

Taking into account the contributions of the two systems considered in Sections 2.2.1 and 2.2.2, the condition of traction free crack surface (2.3) reads

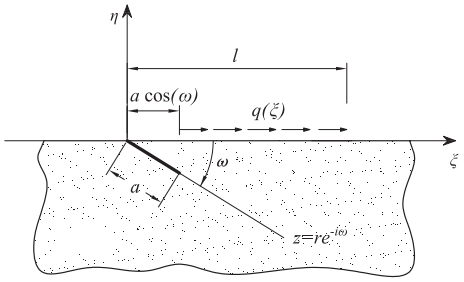

Fig. 11. Elastic half-plane under surface shear stress. Representative variables.

$$\int_0^a B(\rho)K_1(r,\rho)d\rho + \int_0^a \overline{B(\rho)}\left[\frac{2e^{-i\omega}}{r-\rho} + K_2(r,\rho)\right]d\rho + \frac{1}{2\pi}\left[\int_{a\cos\omega}^{l}\overline{q(\xi)}H_1(r,\xi)d\xi + \int_{a\cos\omega}^{l}q(\xi)H_2(r,\xi)d\xi\right] = 0. \tag{3.1}$$

3.1. Approximation in Chebyshev's series

The integral equation (3.1) can be solved using the method suggested by Erdogan and Gupta (1972), which exploits the properties of Chebyshev polynomials of the first and the second kind.[2] These polynomials are traditionally defined in the interval $[-1,1]$, so the variables are transformed according to

$$\rho = \frac{a}{2}(t+1), \tag{3.2a}$$

$$r = \frac{a}{2}(s+1), \tag{3.2b}$$

$$\xi = a\cos\omega + \frac{(l - a\cos\omega)}{2}(\zeta + 1), \tag{3.2c}$$

to obtain

$$\int_{-1}^{1}B(t)K_1(s,t)dt + \int_{-1}^{1}\overline{B(t)}\left[\frac{2e^{-i\omega}}{s-t} + K_2(s,t)\right]d + \frac{1}{2\pi}\left[\int_{-1}^{1}\overline{q(\zeta)}H_1(s,\zeta)d\zeta + \int_{-1}^{1}q(\zeta)H_2(s,\zeta)d\zeta\right] = 0, \tag{3.3}$$

where $K_1(s,t), K_2(s,t), H_1(s,\zeta)$ and $H_2(s,\zeta)$ are reported in Appendix B.

Observe that the kernels $K_1(s,t)$ and $K_2(s,t)$ appearing in the integrals of Eq. (3.3) are not regular at all points of the crack, as can be seen from Eqs. (B.8) and (B.9). They become infinite as both s and t approach the mouth of the crack ($s,t \to -1$). The integral equations are referred to as having Generalized Cauchy kernels and the Gauss Chebyshev quadrature for standard Cauchy integral equations does not apply. It is necessary to examine the behavior of the functions $B(t)$ at the ends $t = \pm 1$.

We argue that at the crack mouth the order of the singularity is weaker than the square root type, and thus we force the dislocation density at the crack mouth to be zero, i.e.,

$$B(-1) = 0. \tag{3.4}$$

It has been demonstrated that such treatment of the mouth of the edge crack produces sufficiently accurate stress intensity factors for the range of angles considered in this study.

For the reasons explained at length in Section 2.1, one can assume that the surface stress $q(\xi)$ is constant over the length l_c, i.e., $q(\xi) = \text{const.} = q$. In this situation, Eq. (3.3) becomes

[2] The definition and properties of Chebyshev polynomials that are used here, have been summarized in the Appendix of Franco and Royer-Carfagni (2014a).

$$\int_{-1}^{1} B(t)K_1(s,t)dt + \int_{-1}^{1} \overline{B(t)}\left[\frac{2e^{-i\omega}}{s-t} + K_2(s,t)\right]dt + \frac{q}{2\pi}\int_{-1}^{1}[H_1(s,\zeta)+H_2(s,\zeta)]d\zeta = 0. \tag{3.5}$$

Such a singular integral equation can be solved by representing the dislocation density $B(t)$ in terms of a bounded (regular) function $B_{\text{reg}}(t)$ and a function $w(t)$ with proper singularities at the end points, of the form

$$B(t) = B_{\text{reg}}(t)w(t) = \frac{B_{\text{reg}}(t)}{\sqrt{1-t^2}}, \tag{3.6}$$

where $B_{\text{reg}}(t)$ is bounded. The regular function can be expressed in terms of the Chebyshev polynomials of the first kind T_j as

$$B_{\text{reg}}(t) = \sum_{j=0}^{n} X_j T_j(t), \tag{3.7}$$

where X_j are *complex* coefficients. Substituting (3.6) and (3.7) in (3.5), setting $\widehat{B}_{\text{reg}} = B_{\text{reg}}/(q_c/(2\pi))$, and using the properties of Chebyshev polynomials, one obtains the discretized form of the integral equation as

$$\frac{\pi}{n}\sum_{k=1}^{n}\widehat{B}_{\text{reg}}(t_k)K_1(s_j,t_k) + \frac{\pi}{n}\sum_{k=1}^{n}\overline{\widehat{B}_{\text{reg}}(t_k)}\left[\frac{2e^{-i\omega}}{s_j-t_k} + K_2(s_j,t_k)\right] + sgn(q)\frac{\pi}{n}\sum_{k=1}^{n}\left[H_1(s_j,\zeta_k)+H_2(s_j,\zeta_k)\right] = 0,$$
$$j = 1,\ldots,n-1, \tag{3.8}$$

where $t_k = \cos\phi_k, s_j = \cos\theta_j$ and $\zeta_k = \cos\delta_k$, while the integration and collocation points

$$\begin{cases} \phi_k = \delta_k = \frac{(2k-1)\pi}{2n} & k = 1,\ldots,n, \\ \theta_j = \frac{j\pi}{n} & j = 1,\ldots,n-1, \end{cases} \tag{3.9}$$

represent the roots of the Chebyshev polynomials of the first and second kind, respectively. The condition

$$\widehat{B}_{\text{reg}}(-1) = 0, \tag{3.10}$$

which satisfies (3.4), renders the system of equations solvable.

3.2. Stress intensity factors

At the tip of the inclined crack, the complex stress intensity factor $K = K_I + iK_{II}$, comprehensive of mode I and mode II opening, is given by

$$K = K_I + iK_{II} = \lim_{r\to a}(\sigma_{\theta\theta} + i\sigma_{r\theta})^{(d+q)}\sqrt{2\pi(r-a)}. \tag{3.11}$$

It can be shown that the only unbounded part of the integral equation (3.1) is the one involving the Cauchy Kernel, so that

$$K = K_I + iK_{II} = \lim_{r\to a}\left[\int_0^a \overline{B(\rho)}\frac{2e^{-i\omega}}{r-\rho}\,d\rho\right]\sqrt{2\pi(r-a)}. \tag{3.12}$$

In terms of the dimensionless quantities introduced in the previous section, Eqs. (3.6) and (3.7), together with the properties[3] of Chebyshev polynomials of the first kind for $|s| > 1$, the relevant expression reads

$$K = K_I + iK_{II} = \frac{q}{2}\sqrt{2\pi a}e^{-i\omega}\sum_{j=0}^{n}\overline{X}_j, \tag{3.13}$$

or, equivalently,

$$K = K_I + iK_{II} = \frac{q}{2}\sqrt{2\pi a}e^{-i\omega}\overline{\widehat{B}_{\text{reg}}}(1), \tag{3.14}$$

which are normalized as

$$K_n = \frac{K}{q\sqrt{2\pi a}} = \frac{1}{2}e^{-i\omega}\sum_{j=0}^{n}\overline{X}_j = \frac{1}{2}e^{-i\omega}\overline{\widehat{B}_{\text{reg}}}(1). \tag{3.15}$$

The value of the function $B(t)$ at the end points $t = \pm 1$ is given by the interpolation formulas (Hills, 1996; Krenk, 1975)

$$B(1) = \frac{1}{n}\sum_{k=1}^{n}\frac{\sin\left[\frac{2k-1}{4n}\pi(2n-1)\right]}{\sin\left[\frac{2k-1}{4n}\pi\right]}B(t_k), \tag{3.16a}$$

$$B(-1) = \frac{1}{n}\sum_{k=1}^{n}\frac{\sin\left[\frac{2k-1}{4n}\pi(2n-1)\right]}{\sin\left[\frac{2k-1}{4n}\pi\right]}B(t_{n+1-k}). \tag{3.16b}$$

Fig. 12 shows the stress intensity factors K_I (Fig. 12(a)) and K_{II} (Fig. 12(b)), evaluated through Eq. (3.14), as a function of the angle ω for different values of the crack length a and a fixed bond length of the stiffener. Both figures have been obtained using the mechanical parameters of Carrara et al. (2011), whose values are reported later in Table 1.

It should be noted that in order to achieve a good approximation of the stress intensity factors the number n of Chebyshev terms strongly increases as ω decreases, i.e., as the crack tends to be parallel to the surface. This is shown in Fig. 13, which plots the normalized stress intensity factors $K_{I,n}$ and $K_{II,n}$, evaluated through Eq. (3.15), as a function of ω for varying n. For the sake of comparison the graph also reports the results obtained using FEM program Abaqus. Observe that, for $\omega > 20°$, 100 terms are sufficient to obtain a very good approximation, but for small values of

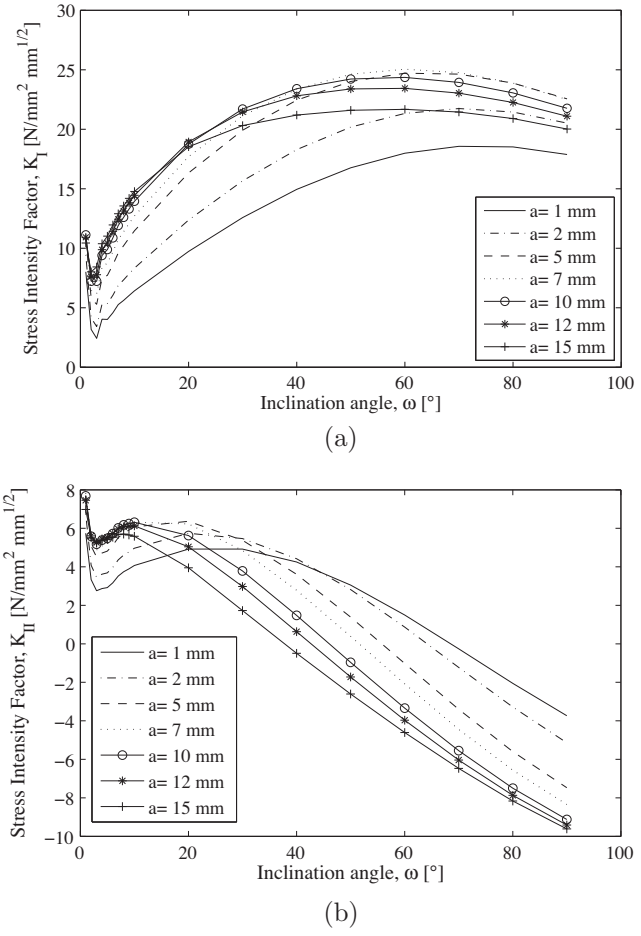

Fig. 12. Stress intensity factors at the tip of the crack for different values of crack length a and a fixed $l = 30$ mm (mechanical properties of Carrara et al. (2011)). Stress intensity factor in: (a) Mode I; (b) Mode II.

[3] See Appendix of Franco and Royer-Carfagni (2014a).

Table 1
Mechanical properties of materials used in experimental campaigns and parameters of the interface law.

Test	Concrete								FRP			Interface law	
	E_p [MPa]	f_t [MPa]	f'_c [MPa]	$d_{a,\max}$ [mm]	W/C –	a_0 –	t_p [mm]	b_p [mm]	E_s [MPa]	t_s [mm]	b_s [mm]	τ_f [MPa]	s_f [mm]
Biolzi et al. (2013)	30500	3.06	32.59	25	0.7	1.00	120	150	170000	1.4	50	7.78	0.26
Carrara et al. (2011)	28700	3.2	32.4	16	0.5	1.44	90	150	168500	1.3	30	7.71	0.15

ω, at least 300 terms are necessary to avoid the classical "fluctuations", as evidenced in Fig. 13(b).

4. Competing mechanisms of failure

In a pull-out test, debonding starts from the loaded end of the stiffener and progresses parallel to its axis (Fig. 1). When the bond length reaches a critical value the formation of an inclined crack at the free end becomes more favorable than continued debonding. There is thus a competition between two different failure mechanisms, summarized in Fig. 14: interface debonding and crack diving into the substrate.

When the interfacial tangential stresses at the loaded end become greater than the maximum allowable tangential stress for the interface, q_0, namely when

$$\tau \geqslant q_0, \tag{4.1}$$

interface debonding occurs and, consequently, fracture propagates parallel to the adhesive joint. We use here a yielding criterion, rather than an energetic criterion à *là* Griffith, because we repute that this is the approach that best interprets the debonding mechanism. In fact, as evidenced in Franco and Royer-Carfagni (2013), consideration of the surface debonding within the framework of Linear Elastic Fracture Mechanics (LEFM) does not allow to completely describe the process. In particular, it is not possible to give a consistent definition of the effective anchorage length because of the presence of stress singularities, which produce a very rapid decay of the contact shear-stress profile at the interface (Franco and Royer-Carfagni, 2013): relative slip and cohesive contact forces are major requirements for a correct interpretation (Franco and Royer-Carfagni, 2014a). Of course, one could relate any cohesive criterion of rupture to an equivalent energetic criterion, but we think that imposing a limit to the shear stress as *per* (4.1) is much simpler and intuitive. As illustrated in Franco and Royer-Carfagni (2014a), the value of q_0 can be determined directly from experimental measurements.

On the other hand, for the inclined crack of length a and inclination ω that progresses from the free end of a stiffener, the energy release rate is obtained from its stress intensity factors by using Irwin's relation

$$G_\omega(a) = \frac{(K_{I,\omega}(a))^2 + \left(K_{II,\omega}(a)^2\right)}{\overline{E}_p}, \tag{4.2}$$

where $\overline{E}_p = E_p$ for plane stress, $\overline{E}_p = E_p/(1-\nu^2)$ for plane strain, and in the notation we have emphasized the dependence upon ω and a. When the crack length passes from the value $a = a_1$ to $a = a_2 > a_1$, the corresponding energy release reads

$$\Delta G_{\omega, a_1 \to a_2} = \int_{a_1}^{a_2} G_\omega(a)\, da. \tag{4.3}$$

One of the major assumptions in the present theory is that fracture propagation is *quantized*, i.e., crack progresses in steps (*quanta*) of finite length, which are of the same order of the material intrinsic

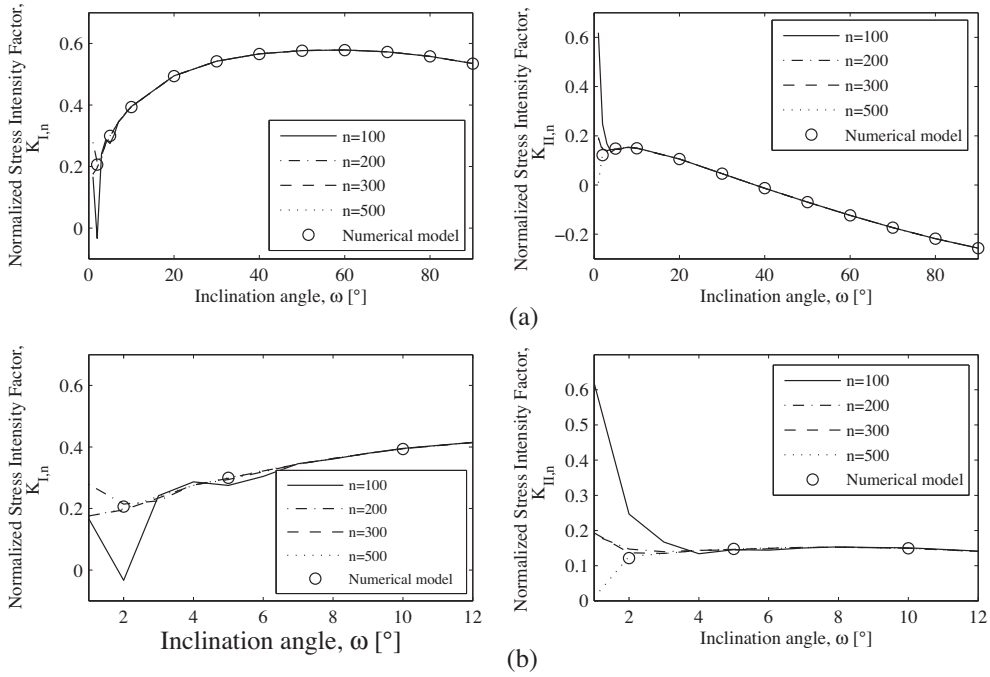

Fig. 13. Normalized stress intensity factors at the tip of the crack as a function of the angle ω (mechanical parameters of Carrara et al. (2011): $l = 30$ mm and $a = 15$ mm). (a) Influence of the number n of terms of the Chebyshev expansion. (b) Detail in the interval $1^\circ \leqslant \omega \leqslant 12^\circ$.

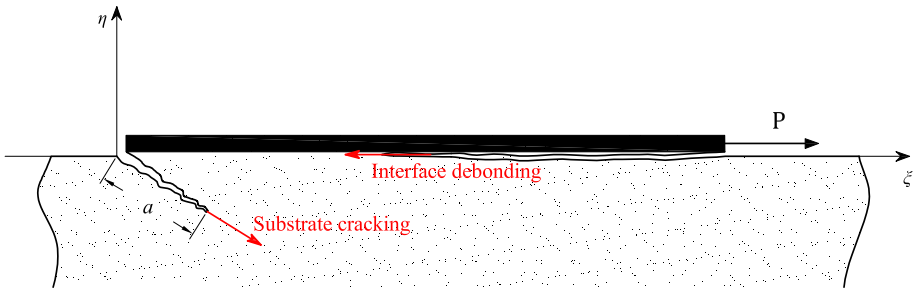

Fig. 14. Competing mechanisms of failure in a pull out test of a stringer bonded to a substrate.

length scale. Let a^* represent such a quantum, and suppose that the toughness of the substrate is defined by the fracture energy *per* unit area Γ. Then, the *quantized nucleation* of the crack at the free end of the stiffener is governed by an energetic balance à *là* Griffith that reads (Li et al., 1995)

$$\int_0^{a^*} G_\omega(a)\,da = \Gamma a^*. \tag{4.4}$$

In such an expression we implicitly assume that the fracture energy is constant, although experimental evidence has shown that the energy dissipated during the first crack jump is usually smaller than that dissipated during later jumps. A variable fracture energy could be incorporated in the proposed model with no major difficulty, but we will not do it because the qualitative description of the process, which is our major aim here, remains unaltered. Therefore, the crack propagates when

$$G^*_\omega \geqslant \Gamma, \quad \text{with} \quad G^*_\omega = \frac{1}{a^*}\int_0^{a^*} G_\omega(a)\,da. \tag{4.5}$$

In general G^*_ω is a quadratic function of the stress intensity factors and, consequently, it is a quadratic function of the shear stress τ transmitted by the stiffener to the substrate. One can normalize such a quantity and write $G^*_\omega = G^*_{\omega,n}\tau^2$, so that Eq. (4.5) can be written in the equivalent form

$$\tau^2 \geqslant \frac{\Gamma}{G^*_{\omega,n}}. \tag{4.6}$$

Comparing this last inequality with (4.1), the competition between the two mechanisms of Fig. 14 can be summarized in the following conditions

$$\begin{cases} \tau^2 \geqslant \Gamma/G^*_{\omega,n}, & \Rightarrow \textit{crack propagation in the substrate}, \\ \tau^2 \geqslant q_0^2, & \Rightarrow \textit{interface debonding}. \end{cases} \tag{4.7}$$

Combining these expressions, following the same rationale proposed by Willis (1967), one obtains

$$\begin{cases} G^*_{\omega,n} q_0^2/\Gamma > 1, & \Rightarrow \textit{crack propagation in the substrate}, \\ G^*_{\omega,n} q_0^2/\Gamma < 1, & \Rightarrow \textit{interface debonding}, \\ G^*_{\omega,n} q_0^2/\Gamma = 1, & \Rightarrow \textit{the two mechanisms are equivalent}. \end{cases} \tag{4.8}$$

The importance of (4.8) is that it provides a comparison which is independent on the applied shear stress τ. The value of the non-dimensional quantity $G^*_{\omega,n} q_0^2/\Gamma$ directly indicates which one of the mechanisms of Fig. 14 is the most favorable when the stiffener is pulled until some damage occurs. When $G^*_{\omega,n} q_0^2/\Gamma$ is less than 1, propagation along the interface (debonding) occurs first; when it is greater than 1, formation of an inclined crack is privileged; when it is equal to 1, both mechanisms are equivalent.

Notice that (4.8) has been derived assuming that the crack surfaces are fully traction free, but in quasi-brittle materials like concrete a fracture process zone (FPZ) does form also at the free end of the stiffener, as discussed in Franco and Royer-Carfagni (2014b). This FPZ has the same effect of an equivalent sharp crack, which may trigger the initiation of the subsurface inclined crack. Indeed, the formal equivalence between Barenblatt and Griffith crack propagation criteria is clearly established in Willis (1967), but under the major assumption that the size of the process zone is small with respect to the size of the crack, which in general is not true for concrete. In any case, this rationale may give reasons for an alternative and equivalent effect to the assumed quantized crack propagation, but this discussion goes beyond the scope of this article.

5. Comparison with experiments

In order to make a comparison with experiments, reference is made to the two campaigns of pull-out tests recorded in Biolzi et al. (2013) and Carrara et al. (2011). Carbon Fiber Reinforced Polymer (CFRP) strips were bonded to concrete prisms and subjected to simple pull out tests with a closed loop control that allowed the capture of snap-back instabilities. Typical specimen size and measured mechanical properties for the materials used in such tests are reported in Table 1.

As already discussed in Section 2.1, it is commonly accepted that the adhesive joint can be characterized by an interface constitutive law of the type represented in Fig. 4, correlating the shear bond-stress τ with the relative slip s of the two adherents through the adhesive. Supposing that the slip between the two adherents is constant in practice, from the constitutive law of Fig. 4 it is possible to consider a definite value for the shear stress transmitted by the stiffener to the substrate. Failure in the bond occurs when such stress reaches the critical value, which has been indicated with q_0 in Section 4.

The correct choice of q_0 deserves some comments. One could directly refer to the peak value τ_f of Fig. 4, which is certainly associated with failure of the interface, but there are some uncertainties in the experimental evaluation of the $\tau - s$ constitutive law. This is assessed by estimating the slip s by measuring, by means of gages, the strains in the stiffener and in the substrate. However, in the latter case the measurement cannot be made immediately below the stiffener, but instead it is made at one of its sides (Ali-Ahmad et al., 2006). Moreover, as evident from Fig. 3, debonding is not a smooth process and the concrete substrate always present noteworthy inhomogeneities that render any constitutive law valid only at the qualitative level.

In the theory of debonding presented in Franco and Royer-Carfagni (2014a,b), a simple step-wise approximation of the constitutive law of Fig. 4 has been sufficient to represent the debonding process in very good agreement with the experimental results. Therefore, one might assume also here $q_0 = \tau_c$, where $\tau_c = \tau_f/2$

represents an average value of the bond strength and corresponds to the maximum stress in a stepwise approximation that preserves the same fracture energy of the joint and the same limit slip s_f. *Ad hoc* experiments would be necessary for a precise evaluation of q_0, but this choice represents a reasonable compromise. In any case, the results that follow remain valid, at the qualitative level, if one considered other values of q_0.

For the experiments of Carrara et al. (2011), the authors suggested the values $\tau_f = 7.71$ MPa and $s_f = 0.15$ mm, so that $\tau_c = 3.85$ MPa (Table 1). Fig. 15 shows the ratio $G^*_{\omega,n}\tau_c^2/\Gamma$ introduced in (4.8), as a function of the inclination angle ω of the crack for different values of the quantum length a^*. The fracture energy Γ for the substrate has been evaluated through the empirical model by Bažant and Becq-Giraudon (2002), which takes into account the effects of the shape and the surface texture of the aggregates based upon a large database of test results. In particular, one can consider the expression for mode I fracture energy of concrete (the dominant fracture mode), which reads

$$\Gamma = 2.5\,a_0\left(\frac{f_c'}{0.051}\right)^{0.46}\left(1+\frac{d_{a,\max}}{11.27}\right)^{0.22}\left(\frac{W}{C}\right)^{-0.30} = \begin{cases} 0.077\ \text{N mm}^{-1}, & \text{for Biolzi et al. (2013)},\\ 0.11\ \text{N mm}^{-1}, & \text{for Carrara et al. (2011)}, \end{cases} \tag{5.1}$$

where a_0 is the parameter that takes into account the shape of the aggregate (1 for rounded aggregates; 1.44 for crushed and sharp aggregates), $f_c' = f_c + 8$[MPa] is the cylinder compressive strength of concrete (NTC, 2008), $d_{a,\max}$ is the maximum aggregate size in the mix and W/C is the water/cement ratio by weight of the mix. Assumed data are listed in Table 1.

The value $G^*_{\omega,n}\tau_c^2/\Gamma = 1$ defines the limit case that separates the two different damage mechanisms as *per* (4.8) of Section 4. From the graph of Fig. 15, it is then possible to evaluate, for a fixed quantum length a^* of crack-propagation, defined in (4.4), the limit angle ω which marks the transition from one of the damage mechanisms to the other. For example, the angle $\omega \simeq 31^\circ$ corresponds to a quantum length $a^* = 10$ mm, whereas the angle $\omega \simeq 21^\circ$ is associated with $a^* = 20$ mm.

For the sake of comparison, we report in Fig. 16 the counterpart of the graphs of Fig. 15 for the case $q_0 = \tau_f$, i.e., when the peak shear stress, rather than the average value, is considered. For this case, $\omega \simeq 33^\circ$ for $a^* = 10$ mm, and $\omega \simeq 26^\circ$ when $a^* = 20$ mm. In general, the higher the value of the critic shear stress q_0, the higher are the inclination angles. It is reasonable to assume that the real

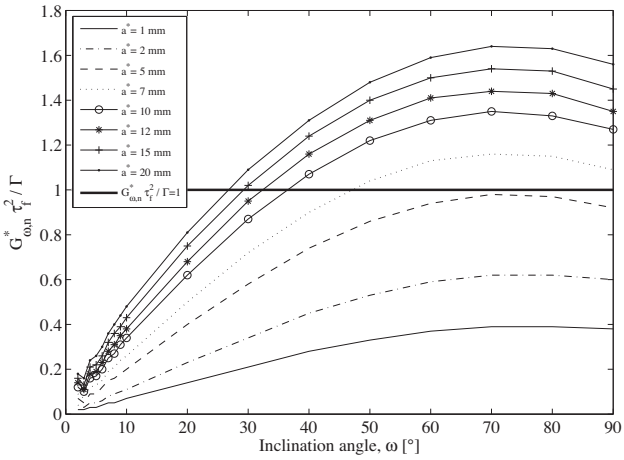

Fig. 16. Normalized strain energy release as a function of the inclination angle ω for different values of the crack quantum length a^* (same parameters of Fig. 15, except $q_0 = \tau_f$ and $l = 25$ mm).

situation should correspond to an intermediate value between $q_0 = \tau_c$ and $q_0 = \tau_f$. However, the qualitative aspects of the problem remain the same.

Fig. 17 reports the counterpart of the graphs of Fig. 16 for the tests by Biolzi et al. (2013). From Table 1, one has $\tau_f = 7.78$ MPa and $s_f = 0.26$ mm. Consequently, for this case, $\omega \simeq 17^\circ$ for $a^* = 10$ mm, and $\omega \simeq 10^\circ$ when $a^* = 20$ mm.

It is important to remark that our results are strongly based upon the assumption of "quantized fracture mechanics" (Pugno and Ruoff, 2004). Relaxation of this hypothesis, i.e., assuming that the crack propagation is smooth and the increment of crack length is infinitesimal, precludes the interpretation of the phenomenon. In fact, notice that as $a^* \to 0$, the corresponding graphs tend to flatten so that in general, for whatever value of ω and q_0, one would find $G^*_{\omega,n}q_0^2/\Gamma < 1$. In other words, interface debonding would always be the preferred mechanism. Therefore, the definition of the "fracture quantum" has a central role for the description of the propagation process.

For the case of concrete, the crack quantum length a^* is of the order of the average size of the aggregate. For the tests of Carrara et al. (2011), since such average size is in the range 10–15 mm, one can conveniently consider values of the same order for

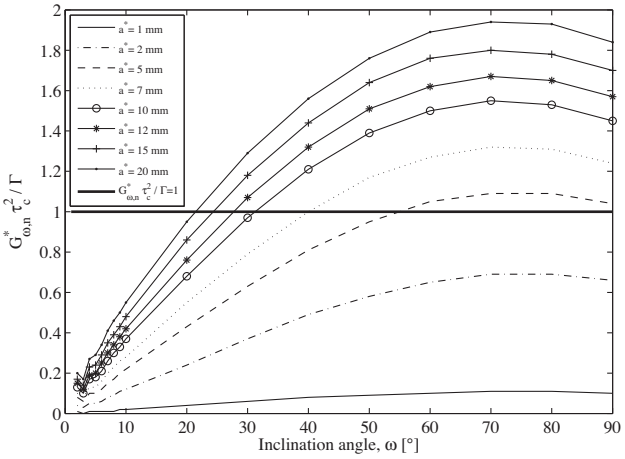

Fig. 15. Normalized strain energy release as a function of the inclination angle ω for different values of the crack quantum length a^* (mechanical parameters of Carrara et al. (2011), bond length $l = 30$ mm, $q_0 = \tau_c$).

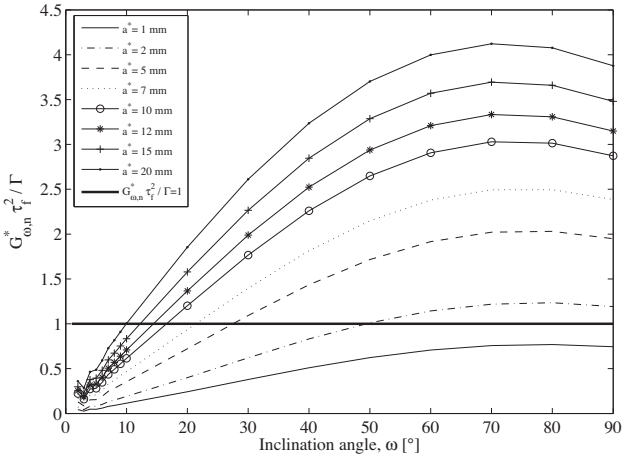

Fig. 17. Normalized strain energy release as a function of the inclination angle ω for different values of the crack quantum length a^* (Mechanical parameters of Biolzi et al. (2013), $l = 50$ mm, $q_0 = \tau_f$).

a^*. Fig. 15 shows that, with this choice, the critical angle ω varies in the interval 24°–31°. From the pictures recorded in Carrara et al. (2011), already presented in Fig. 2, it is evident the formation of wedge-shaped concrete bulbs at the end of the broken specimens. Such wedges are defined by angles comprised in the interval 18°–33°, which agree very well with the conclusions of the present theory.

In the same way, consider the experimental data of Biolzi et al. (2013). One can assume for a^* the average size of the aggregate, which is in the range 10–20 mm. Therefore, from the graph of Fig. 17, it is evident that the critical angle ω varies in the interval 10°–17°. Measurements of the bulbs detached in the experiments (Biolzi et al., 2013) show that the critical angle ω varies in the range 9°–18°, which squares very well with the prediction of the analytical model.

Notice that since the crack quantum length a^* is associated with the characteristic size of the concrete aggregates, the graphs of Fig. 15 are also representative of the size effect due to the substrate microstructure. In other words, the material intrinsic length scale governs the angle of inclination of the wedge-shaped spall. Of course, the size itself of the substrate may also affect the response of the bonded joint, but the model cannot capture this effect because the substrate is assumed to be infinite.

6. Conclusions

The pull-out of a FRP stringer adherent to a quasi-brittle substrate such as concrete is characterized by debonding starting from the loaded end and progressing towards the free extremity of the stringer (Franco and Royer-Carfagni, 2014a,b). A peculiar phenomenon occurs just prior to rupture, when the surviving bond length is of the order of 30–50 mm. An inclined crack forms at the free end of the stiffener and extends into the substrate, and in doing so it defines a wedge-shaped portion of the substrate that eventually separates as a characteristic bulb that remains attached to the stiffener.

To our knowledge, this type of failure has not been exhaustively discussed in the technical literature. This is the motivation for the present study, where a simplified model problem has been presented. The model is built upon four hypotheses: (i) the stiffener bending stiffness is negligible, so that only a tangential traction develops between the stiffener and the substrate; (ii) when the inclined crack initiates, the surviving bond length is so small that the stiffener-substrate relative slip, and consequently the tangential contact stress, can be considered uniform; (iii) the eventual formation of the inclined crack isolates a wedge in the substrate immediately underneath the stiffener that produces a localized release of the stiffener itself, here supposed to be complete (contact stresses directly applied on this portion are neglected); (iv) the crack propagation occurs through crack increments (*quanta*) of small but finite length.

Under the assumption of a linear elastic, homogeneous and isotropic semi-infinite substrate in generalized plane stress, the distributed dislocation approach has been used to determine the opening of the inclined crack, the stress intensity factors, and the energy release rate. The problem is reduced to the solution of a singular integral equation, representing the condition of zero traction along the crack surfaces, which has been solved numerically by using the method proposed by Erdogan and Gupta (1972).

It is concluded that two damage mechanisms are in competition: debonding along the stiffener-substrate interface or cracking at the free extremity of the stiffener along an inclined path. In general, debonding can occur when the shear contact stress is greater than the maximum allowable strength of the interface. On the other hand, the inclined crack opens when the strain energy release associated with its quantized propagation is not lower than the corresponding fracture energy of the substrate itself. Which of the two scenarios is realized for prescribed values of the crack quantum (including the angle of extension of the subsurface crack that do form) is identified using the criterion proposed in Willis (1967).

The hypothesis of "quantized fracture mechanics" is crucial for the present model, because the inclination of the crack that wins the competition with interface debonding depends upon the length of the crack "quantum". This quantity is associated with the characteristic length-scale of the material, which for a natural conglomerate, like concrete, is of the same order of the average size of the aggregate.

Assuming consistent material parameters, the predictions of the proposed model have been compared with experimental results of FRP-to-concrete pull-out tests that are available in the literature. The concrete bulbs that remain attached to the FRP strips have angles in very good agreement with the proposed analytical model. The results of this study provide valuable insights that can in the future be assessed further using computational simulations under less restrictive assumptions. A similar approach might also be used to investigate for the possibility of alternative failure mechanisms in laminated composites under in-plane shear, where the delamination competes with the transverse cracking.

Acknowledgement

The authors acknowledge for partial support the European Community under contract RFSR-CT-2012-00026 (S+G RFS-PR-11017).

Appendix A. The wedge-shaped-cracked half-plane, loaded along the whole bond length of the stiffener

Consider the wedge-shaped cracked elastic half-plane in generalized plane stress of Fig. 5(a), and suppose that the contact stresses with the stiffener are tangential forces per unit area q, uniformly distributed along the *whole* bonded surface. In order to evaluate the state of stress σ_{rr} along such surface, consider the relation

$$\sigma_{rr}+i\sigma_{r\theta}=\Phi(z)+(1+e^{2i\theta})\overline{\Phi(z)}-(z-\bar{z})e^{2i\theta}\overline{\Phi'(z)}+e^{2i\theta}\Phi(\bar{z}). \tag{A.1}$$

With the same procedure of Section 2.2, the stress is due to the superposition of the two problems of Fig. 9.

Consider first the half-plane with the inclined crack (Fig. 10). The stress along the radial line $z=re^{-i\theta}$ due to a distributed dislocation acting along the crack of length a at $z_0=\rho e^{-i\omega}, 0\leqslant\rho\leqslant a$, are given by setting $\Phi(z)=\Phi_{dw}(z)+\Phi_{dc}(z)$, as *per* (2.4) and (2.6), in (A.1), and reads

$$(\sigma_{rr}+i\sigma_{r\theta})^d=\int_0^a B(\rho)K_3(r,\rho)d\rho+\int_0^a\overline{B(\rho)}K_4(r,\rho)d\rho, \tag{A.2}$$

where $K_3(r,\rho)$ and $K_4(r,\rho)$ are given in Appendix B.

The case of a half-space with tangential stresses applied over the length l of its boundary can be solved with the same procedure of Section 2.2 substituting the expression for the complex potentials (2.10) into Eq. (A.1), where in this case the domain of integration is the interval $[0,l]$. The stresses along the line $z=re^{-i\theta}$ due to the presence of a distribution of constant shear stress q along the surface $z_0=\overline{z_0}=\xi$ are given by

$$(\sigma_{rr}+i\sigma_{r\theta})^q=\frac{q}{2\pi}\int_0^l H_3(r,\xi)d\xi, \tag{A.3}$$

where $H_3(r,\xi)$ is given in Appendix B.

Therefore, the state of stress due to the superposed effects is given by

$$\sigma_{rr}+i\sigma_{r\theta}=\int_0^a B(\rho)K_3(r,\rho)d\rho+\int_0^a \overline{B(\rho)}K_4(r,\rho)d\rho+\frac{q}{2\pi}\times\int_0^l H_3(r,\xi)d\xi. \tag{A.4}$$

In the special case $\theta=0$ (surface of the half-plane) the integral (A.4) becomes

$$(\sigma_{rr}+i\sigma_{r\theta})|_{\theta=0}=\int_0^a B(\rho)K_3^*(r,\rho)d\rho+\int_0^a \overline{B(\rho)}K_4^*(r,\rho)d\rho+\frac{q}{2\pi}\int_0^l\left[\frac{4}{\xi-r}\right]d\xi, \tag{A.5}$$

where

$$K_3^*(r,\rho)=\left[2\left(-\frac{1}{r-\rho e^{i\omega}}+\frac{r-\rho e^{i\omega}}{(r-\rho e^{-i\omega})^2}\right)\right],$$
$$K_4^*(r,\rho)=\left[2\left(-\frac{1}{r-\rho e^{-i\omega}}+\frac{r-\rho e^{-i\omega}}{(r-\rho e^{i\omega})^2}\right)\right], \tag{A.6}$$

and the last integral is intended as a Cauchy principal value.

The integral (A.5) can be solved using the methods provided by Erdogan and Gupta (1972) and reported in Section 3.1. By using relations (3.6) and (3.7) and the property of Chebyshev polynomials, one obtains the integral (A.4) in the discretized form

$$(\sigma_{rr}+i\sigma_{r\theta})|_{\theta=0}=\frac{\pi}{n}\sum_{k=1}^{n}B_{\mathrm{reg}}(t_k)K_3^*(s_j,t_k)+\frac{\pi}{n}\sum_{k=1}^{n}\overline{B_{\mathrm{reg}}(t_k)}K_4^*(s_j,t_k)+\frac{q}{2\pi}\left[4\left(i\pi+\ln\left|\frac{1-s_j}{1+s_j}\right|\right)\right],\quad j=1,\dots,n-1, \tag{A.7}$$

where $t_k=\cos\phi_k, s_j=\cos\theta_j$ and the integration and collocation points are given by Eq. (3.9). The following relation holds

$$B_{\mathrm{reg}}=\frac{q}{2\pi}\widehat{B}_{\mathrm{reg}},$$

where $\widehat{B}_{\mathrm{reg}}$ is given by the solution of the integral equation (3.8).

For the sake of comparison, one may focus on the wedge-shaped portion of the substrate isolated by the inclined crack, and consider for this, as an approximation, the solution given by Michell (1899) for an *infinite* wedge loaded by shear stresses on one of its edges, as represented in Fig. 7. Recall that the stress components are given by

$$\sigma_{rr}=-2A_1\cos 2\theta+2A_2-2A_3\sin 2\theta+2A_4\theta, \tag{A.8a}$$
$$\sigma_{r\theta}=2A_1\sin 2\theta-2A_3\cos 2\theta-A_4, \tag{A.8b}$$
$$\sigma_{\theta\theta}=2A_1\cos 2\theta+2A_2+2A_3\sin 2\theta+2A_4\theta, \tag{A.8c}$$

where the four constants can be obtained through the boundary conditions

$$\begin{cases}\sigma_{r\theta}=q, & \sigma_{\theta\theta}=0, \quad \text{for } \theta=0,\\ \sigma_{r\theta}=0, & \sigma_{\theta\theta}=0, \quad \text{for } \theta=\omega.\end{cases} \tag{A.9}$$

The stress components are therefore

$$\sigma_{rr}=-\frac{q}{2}\frac{[\cos(2\theta-\omega)+\cos\omega-2\omega\cos\theta\cos(\theta-2\omega)\csc\omega-2\theta\sin\omega]}{\omega\cos\omega-\sin\omega}, \tag{A.10a}$$
$$\sigma_{r\theta}=-q\frac{[-\cos\theta+\omega\cos\theta\cot\omega+\omega\sin\theta]\sin(\theta-\omega)}{\omega\cos\omega-\sin\omega}, \tag{A.10b}$$
$$\sigma_{\theta\theta}=\frac{q}{2}\frac{[\cos(2\theta-\omega)-\cos\omega-2\omega\sin\theta\sin(\theta-2\omega)\csc\omega+2\theta\sin\omega]}{\omega\cos\omega-\sin\omega}. \tag{A.10c}$$

In the case $\theta=0$, one obtains

$$\sigma_{rr}=\frac{q}{2}\frac{\csc\omega(2\omega\cos 2\omega-\sin 2\omega)}{\omega\cos\omega-\sin\omega}, \tag{A.11a}$$
$$\sigma_{r\theta}=q, \tag{A.11b}$$
$$\sigma_{\theta\theta}=0. \tag{A.11c}$$

Finally, the strain components are given, by Hooke's law, in the form

$$\varepsilon_{rr}=\frac{1}{E}(\sigma_{rr}-\nu\sigma_{\theta\theta}), \tag{A.12a}$$
$$\varepsilon_{\theta\theta}=\frac{1}{E}(\sigma_{\theta\theta}-\nu\sigma_{rr}), \tag{A.12b}$$
$$\varepsilon_{r\theta}=\frac{2(1+\nu)}{E}\sigma_{r\theta}. \tag{A.12c}$$

Remarkably, the simple Michell's solution, and the elastic solution for the cracked half plane, overlap on the wedge-shaped cracked portion, as represented in the graph of Fig. 6.

Appendix B. Green's functions.

Here is a list of the expressions of the Green's functions that are used throughout this article.

$$K_1(r,\rho)=-\frac{2\rho i\sin\omega}{(re^{i\omega}-\rho e^{-i\omega})^2}-\frac{1-e^{-2i\omega}}{(re^{-i\omega}-\rho e^{i\omega})}+\frac{2rie^{-2i\omega}\sin\omega}{(re^{-i\omega}-\rho e^{i\omega})^2} \tag{B.1}$$

$$K_2(r,\rho)=-\frac{1}{(re^{i\omega}-\rho e^{-i\omega})}+\frac{2\rho i(1-e^{-2i\omega})\sin\omega}{(re^{-i\omega}-\rho e^{i\omega})^2}-\frac{e^{-2i\omega}}{(re^{-i\omega}-\rho e^{i\omega})}+\frac{8r\rho e^{-2i\omega}\sin^2\omega}{(re^{-i\omega}-\rho e^{i\omega})^3} \tag{B.2}$$

$$K_3(r,\rho)=-\frac{1}{re^{-i\theta}-\rho e^{i\omega}}+\frac{1}{re^{-i\theta}-\rho e^{-i\omega}}-\frac{1}{re^{i\theta}-\rho e^{-i\omega}}-\frac{e^{2i\theta}}{re^{i\theta}-\rho e^{i\omega}}+\frac{(1+e^{2i\theta})(re^{i\theta}-\rho e^{i\omega})}{(re^{i\theta}-\rho e^{-i\omega})^2}+\frac{4rie^{2i\theta}\sin\theta}{(re^{i\theta}-\rho e^{-i\omega})^2}-\frac{4rie^{2i\theta}\sin\theta(re^{i\theta}-\rho e^{i\omega})}{(re^{i\theta}-\rho e^{-i\omega})^3} \tag{B.3}$$

$$K_4(r,\rho)=-\frac{1}{re^{-i\theta}-\rho e^{i\omega}}-\frac{(1+e^{2i\theta})}{re^{i\theta}-\rho e^{-i\omega}}+\frac{1}{re^{i\theta}-\rho e^{i\omega}}+\frac{re^{-i\theta}-\rho e^{-i\omega}}{re^{-i\theta}-\rho e^{i\omega}}+\frac{2rie^{2i\theta}\sin\omega}{(re^{i\theta}-\rho e^{-i\omega})^2}+\frac{e^{2i\theta}(re^{-i\theta}-\rho e^{-i\omega})}{(re^{i\theta}-\rho e^{i\omega})^2} \tag{B.4}$$

$$H_1(r,\xi)=\frac{1}{\xi-re^{i\omega}}-\frac{e^{-2i\omega}}{\xi-re^{-i\omega}} \tag{B.5}$$

$$H_2(r,\xi)=\frac{(1-e^{-2i\omega})}{\xi-re^{-i\omega}}+\frac{2rie^{-2i\omega}\sin\omega}{(\xi-re^{-i\omega})^2} \tag{B.6}$$

$$H_3(r,\xi)=\frac{1}{\xi-re^{-i\theta}}+\frac{(1+e^{2i\theta})}{\xi-re^{-i\theta}}+\frac{2rie^{2i\theta}\sin\theta}{(\xi-re^{i\theta})^2} \tag{B.7}$$

$$K_1(s,t) = -\frac{2(t+1)i\sin\omega}{\left((s+1)e^{i\omega}-(t+1)e^{-i\omega}\right)^2} - \frac{1-e^{-2i\omega}}{\left((s+1)e^{-i\omega}-(t+1)e^{i\omega}\right)} + \frac{2(s+1)ie^{-2i\omega}\sin\omega}{\left((s+1)e^{-i\omega}-(t+1)e^{i\omega}\right)^2} \tag{B.8}$$

$$K_2(s,t) = -\frac{1}{\left((s+1)e^{i\omega}-(t+1)e^{-i\omega}\right)} + \frac{2(t+1)i(1-e^{-2i\omega})\sin\omega}{\left((s+1)e^{-i\omega}-(t+1)e^{i\omega}\right)^2} - \frac{e^{-2i\omega}}{\left((s+1)e^{-i\omega}-(t+1)e^{i\omega}\right)} + \frac{8(s+1)(t+1)e^{-2i\omega}\sin^2\omega}{\left((s+1)e^{-i\omega}-(t+1)e^{i\omega}\right)^3} \tag{B.9}$$

$$H_1(s,\zeta) = \frac{1}{(\zeta+1)-(s+1)e^{i\omega}} - \frac{e^{-2i\omega}}{(\zeta+1)-(s+1)e^{-i\omega}} \tag{B.10}$$

$$H_2(s,\zeta) = \frac{(1-e^{-2i\omega})}{(\zeta+1)-(s+1)e^{-i\omega}} + \frac{2(s+1)ie^{-2i\omega}\sin\omega}{\left((\zeta+1)-(s+1)e^{-i\omega}\right)^2} \tag{B.11}$$

References

ABAQUS, 2010. Analysis user's manual. Version 6.10, Dassault Systèmes.

Ali-Ahmad, M., Subramaniam, K., Ghosn, M., 2006. Experimental investigation and fracture analysis of debonding between concrete and FRP sheets. J. Eng. Mech. 132, 914–923.

Ballarini, R., Keer, L., Shah, S., 1987. An analytical model for the pull-out of rigid anchors. Int. J. Fract. 33, 75–94.

Ballarini, R., Miller, G., Mukai, D., 1990. Analysis of branched interface cracks. J. Appl. Mech. 57, 887–893.

Bažant, Z.P., Becq-Giraudon, E., 2002. Statistical prediction of fracture parameters of concrete and implications for choice of testing standard. Cem. Concr. Res. 32, 529–556.

Biolzi, L., Ghittoni, C., Fedele, R., Rosati, G., 2013. Experimental and theoretical issues in FRP-concrete bonding. Constr. Build. Mater. 41, 182–190.

Carrara, P., Ferretti, D., Freddi, F., 2013. Debonding behavior of ancient masonry elements strengthened with CFRP sheets. Composites B: Eng. 45, 800–810.

Carrara, P., Ferretti, D., Freddi, F., Rosati, G., 2011. Shear tests of carbon fiber plates bonded to concrete with control of snap-back. Eng. Fract. Mech. 78, 2663–2678.

Chen, J., Teng, J., 2001. Anchorage strength models for FRP and steel plates bonded to concrete. J. Struct. Eng. 127, 784–791.

CNR-DT/200, 2004. Guide for the Design and Construction of Externally Bonded FRP Systems for Strengthening Existing Structures – Materials, RC and PC structures, masonry structures. National Research Council (CNR).

Dundurs, J., 1969. Mathematical Theory of Dislocations. American Society of Mechanical Engineers (Elastic interaction of dislocations with inhomogeneities).

Erdogan, F., Gupta, G.D., 1972. On the numerical solution of singular integral equations. Q. Appl. Math. 29, 525–534.

Eshelby, J., Frank, F., Nabarro, F., 1951. XLI. The equilibrium of linear arrays of dislocations. Philos. Mag. 42, 351–364.

Franco, A., Royer-Carfagni, G., 2013. Energetic balance in the debonding of a reinforcing stringer: Effect of the substrate elasticity. Int. J. Solids Struct. 50, 1954–1965.

Franco, A., Royer-Carfagni, G., 2014a. Cohesive debonding of a stiffener from an elastic substrate. Composites Struct. 111, 401–414.

Franco, A., Royer-Carfagni, G., 2014b. Effective bond length of FRP stiffeners. Int. J. Non-Linear Mech. 60, 46–57.

Freddi, F., Savoia, M., 2008. Analysis of FRP-concrete debonding via boundary integral equations. Eng. Fract. Mech. 75, 1666–1683.

Grande, E., Imbimbo, M., Sacco, E., 2011. Bond behaviour of CFRP laminates glued on clay bricks: experimental and numerical study. Composites B: Eng. 42, 330–340.

He, M., Hutchinson, J., 1988. Kinking of a crack out of an interface. J. Appl. Mech. 56, 270–278.

Hills, D., 1996. Solution of Crack Problems: The Distributed Dislocation Technique. Mathematics and Its Applications. Springer.

Krenk, S., 1975. On the use of the interpolation polynomial for solutions of singular integral equations. Q. Appl. Math. 32, 479–484.

Le, J.L., Bažant, Z.P., Yu, Q., 2010. Scaling of strength of metal-composite joints-part ii: interface fracture analysis. J. Appl. Mech. 77, 011012-1–011012-7.

Li, Y., Hong, A., Bažant, Z., 1995. Initiation of parallel cracks from surface of elastic half-plane. Int. J. Fract. 69, 357–369.

Marfia, S., Sacco, E., Toti, J., 2011. A coupled interface-body nonlocal damage model for the analysis of FRP strengthening detachment from cohesive material. Frattura ed Integrità Strutturale 18, 23–33.

Mazzotti, C., Savoia, M., Ferracuti, B., 2009. A new single-shear set-up for stable debonding of FRP-concrete joints. Constr. Build. Mater. 23, 1529–1537, FRP Composites in Construction.

Michell, J.H., 1899. On the direct determination of stress in an elastic solid, with application to the theory of plates. Proc. London Math. Soc. 31, 100–124.

Muskhelishvili, N., 1975. Some Basic Problems of the Mathematical Theory of Elasticity. 1. Noordhoff.

NTC, 2008. New Technical standards for Construction. Italian Ministry of Public Works (DM 14.01.08). In Italian.

Pellegrino, C., Tinazzi, D., Modena, C., 2008. Experimental study on bond behavior between concrete and FRP reinforcement. J. Compos. Constr. 12, 180–189.

Pugno, N.M., Ruoff, R.S., 2004. Quantized fracture mechanics. Philos. Mag. 84, 2829–2845.

Willis, J., 1967. A comparison of the fracture criteria of Griffith and Barenblatt. J. Mech. Phys. Solids 15, 151–162.

Yuan, H., Teng, J., Seracino, R., Wu, Z., Yao, J., 2004. Full-range behavior of FRP-to-concrete bonded joints. Eng. Struct. 26, 553–565.